Toward the Discrimination of Oil Spills in Newly Formed Sea Ice Using C-Band Radar Polarimetric Parameters

Elvis Asihene, *Graduate Student Member, IEEE*, Gary Stern, David G. Barber,
Colin Gilmore, *Senior Member, IEEE*, and Dustin Isleifson, *Senior Member, IEEE*

Abstract— Climate-driven sea ice loss has exposed the Arctic to increased human activity, which comes along with a higher risk of oil spills. As a result, we investigated the ability of C-band polarimetric parameters in a controlled mesocosm to accurately identify and discriminate between oil-contaminated and uncontaminated newly formed sea ice (NI). Parameters, such as total power, copolarization ratio, copolarization correlation coefficient, and others, were derived from the normalized radar cross section and covariance matrix to characterize the temporal evolution of NI before and after oil spill events. For separation purposes, entropy (H) and mean-alpha (α) were extracted from eigen decomposition of the coherency matrix. The H versus α scatterplot revealed that a threshold classifier of 0.3-H and 18°-α could distinguish oil-contaminated NI from its oil-free surroundings. From the temporal evolution of the polarimetric parameters, the results demonstrate that the copolarization correlation coefficient is the most reliable polarimetric parameter for oil spill detection, as it provides information on a variety of oil spill scenarios, including oil encapsulated within ice and oil spreading on top of ice. Overall, these findings will be used to support existing and future C-band polarimetric radar satellites for resolving ambiguities associated with Arctic oil spill events, particularly during freeze-up seasons.

Index Terms— Arctic, discrimination, eigen decomposition, oil spill, polarimetric parameter, radar, sea ice.

I. INTRODUCTION

ACCURATE detection of oil spills in the Arctic ice-laden waters is critical, as climate-driven reductions in sea ice thickness and concentration have increased marine operations in the region, including vessel navigation and natural resource extraction [1], [2], [3], [4]. To monitor

marine oil pollution, a combination of satellite- and aircraft-based single polarization active microwave remote sensing [e.g., synthetic aperture radar (SAR) and scatterometer] has been used to detect low backscatter areas caused by oil dampening ocean surface waves that scatter in the Bragg limits [5], [6], [7]. However, in ice-laden waters, the distribution of sea ice, particularly newly formed sea ice (NI) types, such as frazil, grease ice, and nilas, complicates the detection of oil spills due to their low backscatter response [8]. Using polarimetric radar may improve the discrimination between oil-contaminated and uncontaminated NI, allowing for correct identification of when and where oil is spilled.

In a polarimetric radar system, it is possible to mathematically combine multipolarization backscatter responses to derive polarimetric parameters that increase contrast between different scattering mechanisms. However, the use of polarimetric parameters for discriminating oil spills in ice-laden waters has not yet been fully established. Parameters, such as total power (SPAN), copolarization ratio (R_{co}), cross-polarization ratio (R_{xo}), copolarization difference (PD), copolarization correlation coefficient (ρ_{co}), entropy (H), and mean-alpha (α), have seen limited use (e.g., [8], [9], [10]). Other parameters, including conformity coefficient (μ) and geometric intensity (ν), to the best of our knowledge, have not been presented in the peer-reviewed literature. We refer to Section II-C for a detailed explanation of these polarimetric parameters, as well as their derivation and physical meaning.

Among the few recent studies to establish polarimetric radar as a means for detecting oil in sea ice, Brekke et al. [8] simulated the R_{co} values and used them to distinguish between uncontaminated and oil-contaminated NI. Because the R_{co}-parameter exhibits some separation capability, additional studies evaluated its performance with the H, α, and PD parameters on pairs of SAR images; one containing oil-contaminated open water (OW) and the other, oil-free NI [9], [10]. With the exception of the PD-parameter, the results showed that the R_{co}, H, and α parameters at lower incidence angle ($<35°$) have the greatest separability between oil-contaminated OW and NI, but the paired image lacks comparable geographic reference, and their applicability is limited to only oil-contaminated OW between ice-laden waters. Apart from oil-in-sea ice research, previous literature

Elvis Asihene, Gary Stern, and David G. Barber are with the Centre for Earth Observation Science (CEOS), University of Manitoba, Winnipeg, MB R3T 5V6, Canada (e-mail: asihene@myumanitoba.ca).

Colin Gilmore is with the Department of Electrical and Computer Engineering, University of Manitoba, Winnipeg, MB R3T 5V6, Canada.

Dustin Isleifson is with the Centre for Earth Observation Science (CEOS) and the Department of Electrical and Computer Engineering, University of Manitoba, Winnipeg, MB R3T 5V6, Canada.

has shown the potential of ρ_{co}, μ, and ν parameters in distinguishing between oil-contaminated and uncontaminated OW [11], [121], [13], [14], [15], as well as the use of SPAN, ρ_{co}, and R_{xo} parameters in classifying different NI types [16], [17], [18], [19]. However, to the best of our knowledge, no attempt has been made to use C-band polarimetric radar to discriminate between oil within or on sea ice; thus, prompting our investigation.

NI is a complex heterogeneous material made up of high volume of liquid brine and to a lesser extent, air inclusions in a pure ice background. During its initial formation, the topmost layer is highly saline, causing the surface to be brine-wetted or covered with frost flowers, when given favorable atmospheric conditions [20]. Because of the dynamic environmental conditions of the Arctic region, the geophysical and thermodynamic states of NI undergo rapid change, making its backscattering response highly variable [18]. Moreover, the introduction of oil below, within, and on the ice is expected to add to its already complicated backscattering behavior [21]. When oil is distributed beneath the ice under quiescent freezing conditions, it slowly infiltrates the ice–water interface and migrates through the ice medium until it becomes encapsulated [22], [23], [24]. This encapsulation event can occur rapidly due to a low oil volume fraction (<2%) [25], [26] or due to granular brine pockets within the ice topmost layer [24]. If the ice temperature begins to warm, the oil migrates onto the ice surface [22], [23], [24], [25], [26], which in turn reduces the backscatter responses [27], [28], [29], [30], [31]. Prior to the oil migration on the ice surface, previous studies in [31] found that the copolarized backscatter increases with a coincident decrease in cross polarization. As such, we expect that when oil migrates onto the ice surface (or its near surface), the time-series response of polarimetric parameters will be uniquely sensitive.

Polarimetric radar response of a homogenous level sea ice is dominated by a complex combination of surface and volume scattering mechanisms. The former is caused by small-scale roughness on the sea–ice interface (e.g., air–ice interface), while the latter is caused by the heterogeneity within the sea ice medium [17]. These scattering mechanisms can be separated using target decomposition (TD) theorems, which are extensively discussed in [32]. Among the various TD theorems, Cloude's eigen-based decomposition method will be used in this study because it allows for the derivation of H and α parameters required for natural terrain classification [33]. The H-parameter measures a medium's scattering inhomogeneity, whereas the α-parameter measures the dominant scattering mechanism, and when related, they provide the framework for separating several natural terrains, including homogenous level sea ice, which was classified as surface scattering low entropy (SSLE) [33]. We hypothesize that oil-contaminated NI will fall within the SSLE zone, but it will cluster separately from the uncontaminated ones. This is because we expect oil to modify the ice volume dielectrics via thermophysical processes [22], [23], [24], [25], [26], [34], as well as the ice surface dielectric via a dampening effect [28], [29], [31]. Thus, we suggest that setting a threshold of H and α parameters within the SSLE zone may be useful in identifying oil spills in NI.

The main objective of this study is to investigate the potential of C-band polarimetric parameters for discriminating oil spills in NI types, such as dark nilas and light nilas, in relation to their scattering mechanisms. To achieve this, we will derive eight well-known polarimetric parameters from surface-based C-band polarimetric scatterometer data that were initially presented in [31]. As such, this manuscript extends the interpretation in [31] and is the first attempt toward using ground-truth scatterometer data to assess the optimum polarimetric parameters for oil in sea ice discrimination. On the basis of our analysis, we pose two novel research questions.

1) Which time-series responses of SPAN, R_{co}, R_{xo}, ρ_{co}, μ, and ν of NI is the most sensitive to an oil within or on ice spill event?

2) Is it possible to effectively separate oil-contaminated NI from oil-free NI by using the relationship between H and α parameters?

The remainder of this manuscript is organized as follows. Section II provides an overview of the experimental site and data description, as well as how the polarimetric parameters and threshold classifier were derived. Section III presents the results of the derived polarimetric parameters. In addition, we demonstrated the threshold classifier results on trained and tested datasets. Section IV discusses the discrimination analysis, and Section V concludes with a summary and recommendations.

II. MATERIAL AND METHODS

A. Experimental Site

The experimental site for this study is located in Canada at the University of Manitoba's Sea-ice Environmental Research Facility (SERF; e.g., see [20], [28], [29], [31], [35], [36]). In February 2020, two phases of experiment were carried out in two separate cylindrical tubs at the outdoor facility [31]. Phase-1 began at midnight on February 7 and lasted approximately 40 h, during which oil was injected beneath an established ice, which grew (7.5 cm thick) from artificial seawater in a 13-m^3 uninsulated cylindrical tub. Phase-2 began at 4 PM on February 12 and lasted 19 h, involving an ice regrowth (5 cm thick) that follows the melting of the existing oil-contaminated ice in phase-1. For control purposes, we developed an oil-free ice (8 cm thick) using a 9-m^3 fiberglass-insulated cylindrical tub in close proximity to the oil experimental tub. Each tub was outfitted with thermocouple strings through a polyvinyl chloride pipe, and a scatterometer was mounted on a nearby scaffolding tower at a height of 5.3 m above the seawater surface. In a separate study (February 2021), we used a different experimental setup with the SERF main pool (see detailed descriptions in [20], [35], and [36]), in the absence of oil contamination. These experimental results are used to verify the robustness of our proposed threshold classifier (see Section II-D).

B. Data Description

Meteorological data, in situ physical sampling data, LiDAR/UAV data, and scatterometer data were all collected

during phases 1 and 2 experiments. The full explanation of these datasets can be found in [31]; however, we describe herein a summary of how oil on the ice surface influenced the ice geophysical and thermodynamic states, as well as the ice backscattering response.

1) Meteorological Data: Mean hourly measurements of atmospheric pressure, shortwave irradiance, and temperature were taken from a meteorological station positioned 15 m away from the experimental tubs, characterizing the local weather conditions prior to, and post, oil injection. Although no quantitative wind speed or direction data were collected directly over the tubs, we observed a very calm wind effect, and the ice grew in a quiescent state. The atmospheric pressure in phase-1 was relatively close to the standard atmospheric pressure (101.325 kPa), while it was slightly higher in phase-2. In both experiments, the downwelling shortwave irradiance was constant, with some localized major spikes. For the phase-1 experiment, the air temperature fluctuated from -22 °C to -9 °C, whereas the ice surface temperature followed a similar trend but was on average 8 °C warmer. At 32 h, a steady increase in air temperature initiated the migration of mixed brine and oil onto the ice surface (see the associated microwave scattering in Section II-B4). Throughout the phase-2 experiment, the air and ice surface temperatures remained relatively constant at -23 °C and -17 °C, respectively.

2) Physical Sampling Data: The physical sampling data, consisting of salinity, ice volume temperature, and ice thickness, were obtained from the sampled ice cores to characterize their geophysical and thermodynamic states. The ice cores sampled during the phase-1 experiment revealed a continuous ice growth, which were highly saline at the topmost layer and had a low oil-volume fraction (0.7%) when the oil migrated onto the ice surface in the oil tub. For the phase-2 experiment, the ice core from the oil tub had a higher oil-volume fraction (3%). This resulted in a 29% and 20% decrease in the ice growth rate and surface salinity, respectively, when compared to the corresponding control tub.

3) LiDAR/UAV Data: The LiDAR and UAV datasets were only collected during the phase-1 experiment to characterize the ice surface roughness. Prior to, and following, the oil injection, the data showed that the ice surface was slightly rough according to Fraunhofer roughness criterion [37].

4) Scatterometer Data: The polarimetric normalized radar cross section (NRCS) was calculated from C-band scatterometer data to establish the ice radar backscattering at 22.5° incidence angle from the control tub and 24.5° incidence angle from the oil tub. We chose these incidence angles due to the constraints imposed by the tub size (i.e., these angles were not affected by the tub edges). Prior to data collection, we performed a corner reflector calibration routine for our scatterometer system to determine the optimal backscatter response [38]. A total of 422 scatterometer samples were collected for phases 1 and 2 experiments: 201 from the phase-1 oil tub, 98 from the phase-1 control tub, and 123 from the phase-2 oil tub.

During the phase-1 experiment, in the oil tub, two local scattering maxima were observed in the time-series response

TABLE I
DEFINITION OF ICE REGIMES IN RELATION TO THE TIME-SERIES RESPONSE OF C-BAND POLARIMETRIC NRCS DURING PHASE 1 EXPERIMENT

Oil Tub	
I	Open water + Frazil
II	Oil-free dark nilas
III	Oil-free dark nilas*
IV	Oil contaminated light nilas
V	Oil contaminated light nilas**
Control Tub	
II+III	Oil-free dark nilas
IV+V	Oil-free light nilas

* indicates that the ice regime-III is physically contaminated with oil, but the C-band NRCS response was undetected by the oil inclusion (see Fig. 1).
** indicates that the presence of oil on the ice surface during the ice regime V.

of the copolarized NRCS (see Fig. 1, left). The first maximum occurred prior to the oil injection and was associated with a rapid surface brine expulsion. The second maximum occurred immediately before oil migrated onto the ice surface and was attributed to a combined effect of upward brine expulsion and oil migration, resulting in a distinctive backscattering response of oil on the ice surface [30]. Five distinct ice regimes were identified and characterized by relating the ice backscattering response to its physical state, as described in Table I. In contrast to the oil tub, we identified two ice regimes in the control tub (see Fig. 1, middle). We configured the scatterometer to scan over the oil tub for the first eight hours and then alternated between tubs approximately every hour [30]. In the phase-2 experiment (only oil tub), the time-series response of the polarimetric NRCS was relatively constant at lower magnitudes (<-35 dB, see Fig. 1, right), indicating a specular reflection despite the ice growing beneath an oil layer.

C. Derivation of Polarimetric Parameters

The polarimetric radar response of NI can have many variations based on the specific physical conditions of the ice. We calculated the polarimetric parameters by spatially averaging 39 independent samples within a 10° azimuthal width. During the spatial averaging process, a $\pm 3\Delta R$ range window was used, where ΔR is the scatterometer range resolution (30 cm) [39]. To better describe, the full scattering mechanism requires a statistical approach, in which the directly measured 2×2 scattering matrix is translated into a second-order 4×4 matrix, such as the covariance matrix $[C_4]$ and the coherency matrix $[T_4]$. These matrices were included in the scatterometer data products, and we reduced them to 3×3 averaged matrices for a monostatic configuration, as expressed in [32], (1) and (2), as shown at the bottom of the next page, where $\langle \cdot \rangle$ represents the spatial ensemble averaging operator and superscript $*$ represents the complex conjugate. S_{vh} is the complex scattering element of vertical (v) transmitting and horizontal (h) receiving polarizations, while S_{vv}, S_{hh}, and S_{hv} are defined in similar routine. Although both elements in $[C_3]$ and $[T_3]$ describe the statistical scattering process, the elements in $[T_3]$ are much more physically meaningful due to their close association with the physical and geometrical properties of the natural terrain surfaces [33], [40], [41]. As a result, the diagonal elements in (2)
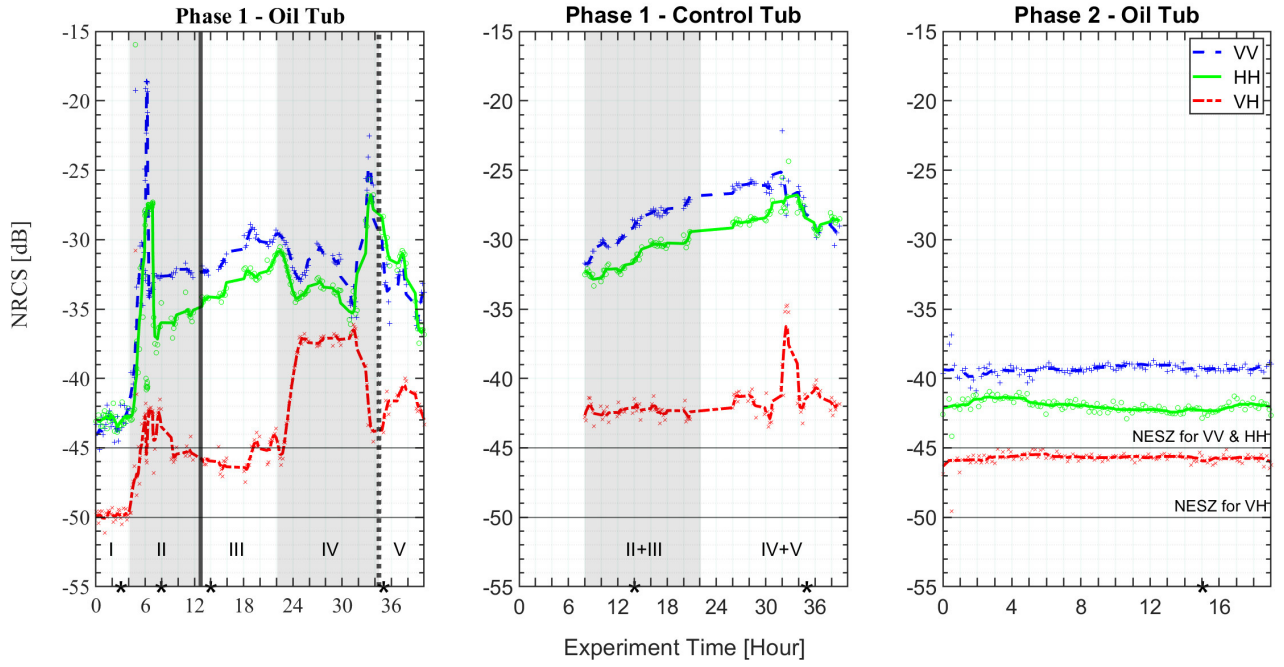
Fig. 1. Time-series response of polarimetric NRCS measured during phases 1 and 2 experiments at 22.5° incidence angle on the control tub and 24.5° incidence angle on the oil tub. Markers show the raw measured data with corresponding best-fit lines. The black vertical line illustrates the period when oil was injected beneath the sea ice, and the vertical dotted line shows the period when the initial oil migrated onto the ice surface. Backscattering responses in phase-1 oil tub were categorized into five regimes (I–V) based on the sampled ice thickness, when oil was injected beneath the ice, and when oil migrated on the ice surface, whereas phase-1 control tub was categorized into two groups of ice regimes (II + III and IV + V) based on their sampled ice thickness. On the x-axis, the asterisks indicate the sampling hours for ice cores; their average thicknesses are I = 1.8 cm, II = 3.4 cm, III = 5 cm, and V = 7.5 cm in phase 1 oil tub, II + III = 5 cm and IV + V = 8 cm in phase 1 control tub, and 5 cm in phase 2 oil tub (see details in [31]). The horizontal lines at −45 and −50 dB represent the NESZ for copolarized and cross-polarized NRCS, respectively.

correspond to contributions from surface scattering, double-bounce scattering, and volume scattering, respectively [32].

Under calm conditions, the scattering mechanism of homogenous level NI can be described as surface scattering or as both surface and volume scattering if the sea ice is covered with snow (mostly, in wet snow) [42]. All elements correlated with double-bounce scattering are negligibly small [42] and, thus, must be approximated to zero in order to accurately model both the surface and volume scattering behaviors from the coherency matrix in (2). This is achieved as follows:

$$\langle [\widetilde{T_3}] \rangle = \frac{1}{2} \begin{bmatrix} \langle |S_{vv} + S_{hh}|^2 \rangle & \sim 0 & 2\langle (S_{vv} + S_{hh})S_{vh}^* \rangle \\ \sim 0 & \sim 0 & \sim 0 \\ 2\langle S_{vh}(S_{vv} + S_{hh})^* \rangle & \sim 0 & 4\langle |S_{vh}|^2 \rangle \end{bmatrix}$$
$$(3)$$

where $\langle [\widetilde{T_3}] \rangle$ represents the 3×3 averaged coherency matrix after minimizing the double-bounce scattering effect. It is worth noting that the symbol, $\sim$ assigned to these

approximated elements signifies that 0 is equivalent to 10^{-6} in order to avoid matrix singularity.

Polarimetric parameters, including R_{co} and R_{xo}, are derived from the NRCS; SPAN, ρ_{co}, and μ are derived from $\langle [C_3] \rangle$ in (1); and ν is derived from $\langle [T_3] \rangle$ in (2). Additional polarimetric parameters, such as H and α, are derived from eigen decomposition of $\langle [\widetilde{T_3}] \rangle$ in (3). Formulations of these are expressed in Table II.

The SPAN parameter measures the total backscatter response [16]. We expect it to be less sensitive to changes in scattering mechanisms. For example, a study in [43] has shown that it becomes less sensitive to volume scattering of sea ice as the incidence angle increases in the C-band frequency.

The R_{co}-parameter is sensitive to changes in surface scattering (e.g., bare sea ice [44]), which increases with increasing incidence angle [8], [9]. Meanwhile, R_{xo} is strongly associated with changes in volume scattering [45]. As such, any depolarization effect within a homogenous ice volume is expected to enhance the R_{xo}-parameter (e.g., brine pocket

$$\langle [C_3] \rangle = \begin{bmatrix} \langle |S_{vv}|^2 \rangle & \sqrt{2}\langle S_{vv}S_{vh}^* \rangle & \langle S_{vv}S_{hh}^* \rangle \\ \sqrt{2}\langle S_{vh}S_{vv}^* \rangle & 2\langle |S_{vh}|^2 \rangle & \sqrt{2}\langle S_{vh}S_{hh}^* \rangle \\ \langle S_{hh}S_{vv}^* \rangle & \sqrt{2}\langle S_{hh}S_{vh}^* \rangle & \langle |S_{hh}|^2 \rangle \end{bmatrix}$$
$$(1)$$

$$\langle [T_3] \rangle = \frac{1}{2} \begin{bmatrix} \langle |S_{vv} + S_{hh}|^2 \rangle & \langle (S_{vv} + S_{hh})(S_{vv} - S_{hh})^* \rangle & 2\langle (S_{vv} + S_{hh})S_{vh}^* \rangle \\ \langle (S_{vv} - S_{hh})(S_{vv} + S_{hh})^* \rangle & \langle |S_{vv} - S_{hh}|^2 \rangle & 2\langle (S_{vv} - S_{hh})S_{vh}^* \rangle \\ 2\langle S_{vh}(S_{vv} + S_{hh})^* \rangle & 2\langle S_{vh}(S_{vv} - S_{hh})^* \rangle & 4\langle |S_{vh}|^2 \rangle \end{bmatrix}$$
$$(2)$$

TABLE II
INVESTIGATED POLARIMETRIC PARAMETERS
AND THEIR FORMULATIONS

$SPAN = $ $10\,log_{10}[\langle|S_{vv}|^2\rangle + 2\langle|S_{vh}|^2\rangle + \langle|S_{hh}|^2\rangle]$	$\rho_{co} = \left\|\dfrac{\langle S_{vv}S_{hh}^{*}\rangle}{\sqrt{\langle|S_{vv}|^2\rangle\langle|S_{hh}|^2\rangle}}\right\|$
$R_{co} = 10\log_{10}\left[\dfrac{\sigma_{vv}^{\;2}}{\sigma_{hh}^{\;2}}\right]$	$\mu = \dfrac{2\left[\text{Re}\langle S_{vv}S_{hh}^{*}\rangle - \langle|S_{vh}|^2\rangle\right]}{\langle|S_{vv}|^2\rangle + 2\langle|S_{vh}|^2\rangle + \langle|S_{hh}|^2\rangle}$
$R_{xo} = 10\log_{10}\left[\dfrac{\sigma_{vh}^{\;2}}{\sigma_{hh}^{\;2}}\right]$	$\alpha = \sum\limits_{i=1}^{3} P_i \cos^{-1}(|\bar{u}_i|)$
$\nu = 10\log_{10}\sqrt[3]{\det|\langle[\widetilde{\mathbf{T}_3}]\rangle|}$	$H = -\sum\limits_{i=1}^{3} P_i \log_3 P_i$

Where σ_{vv}, σ_{vh} and σ_{hh} represent the NRCS in the vv, vh, and hh polarizations, respectively. See [33] for the derivatives of pseudoprobabilities, Pi (which are related to the eigenvalues), and eigenvectors, $\bar{u}_i$ of coherency matrix.

rearrangements within sea ice volume [16] or oil movement within the ice volume [31]).

The ν-parameter is associated with the geometric mean of the eigenvalues of $\langle[T_3]\rangle$ [46], [47]. Because it contains information about cross products between copolarized backscattering element, we expect it to be sensitive to depolarization effects within the ice volume.

The ρ_{co}-parameter ranges from 0 to 1. During a continuous sea ice growth, it approaches 1, making it useful for distinguishing between NI with thicknesses <6 cm and >8 cm in the C-band microwave frequency range [18]. When ρ_{co} approaches 0, it is expected that inhomogeneities within the sea ice will be discernable (e.g., anisotropic distribution of brine pockets [48] or oil-in-sea ice encapsulation [31]). Meanwhile, the μ-parameter is an indicator that assigns positive and negative values to slightly rough and smooth surfaces, respectively [12]. Based on the formulation of the μ-parameter in Table I, it is contrasting the correlation between the copolarized scattering responses and a sensor-dependent threshold that is typically provided by the cross-polarized scattering response. This μ-parameter ranges from -1 to 1 and has been reported to provide an excellent measure to discriminate oil-contaminated OW from the oil-free ocean surroundings [12]. Based on the past studies, we expect a low ρ_{co} values [11] and negative μ values [12] when oil migrates through the topmost layer of the ice or when oil covers the ice surface.

The H and α parameters extracted from eigen decomposition of $\langle[\widetilde{T_3}]\rangle$ can be used as a powerful tool for unsupervised natural terrain classification. This method of classification was first reviewed in [40] and applied in [33], where polarimetric SAR imagery of various natural terrain was segmented into eight zones [33]. In [49], similar analysis was used to distinguish different sea ice types, with bare seasonal ice classified as SSLE zone. We intend to extend this H/α classification criterion in an oil-contaminated NI situation. However, the disadvantage is that the classification will be degraded due to the large radar footprint from the inherent sampling of polarimetric SAR [39]. This means that the

SAR footprint contains a variety of terrain types, making it difficult to directly relate the pure homogenous area to its geophysical properties. With ground-truth scatterometer measurements, it is possible to achieve sampling homogeneity, which links the polarimetric backscatter to its geophysical properties [39], and thus obtain a better physical interpretation for the H and α parameters. Another issue is that the linearly fixed boundaries in the H/α plane oversimplify the classification, as multiple clusters with distinct geophysical properties may fall into the same zone [50]. To refine this classification into subclasses, studies in [51] included a new parameter called anisotropy, which was found to be effective in separating highly random surfaces enclosed in the same zone. Another refinement approach is to use fuzzy logic techniques, which have been shown to be successful for complex natural terrain types [52]. Despite the benefits of these refinement techniques, major obstacles remain for NI classification due to its predominately homogenous and undeformed surface. Outside of the H/α plane, some sea ice analysts (e.g., [53], [54] and references therein) directly applied NRCS thresholds to different sea ice types, and it is currently used by the Canadian Ice Service for shipping navigation within the Canada's Arctic territory [55]. Here, our motivation is to leverage the threshold classification scheme within the H/α SSLE zone to characterize the scattering behavior of NI terrain. As such, we anticipate that if NI becomes contaminated with oil, it will fall within the SSLE zone.

D. Threshold Classifier Algorithm

Our proposed threshold classifier is simple to implement, adaptable to changing environmental conditions, and effective for homogenous-level NI terrain. Fig. 2 illustrates how the threshold classifier algorithm works. First, we extract the H and α parameters from the eigen decomposition of the coherency matrix data. Next, we apply the H/α classification scheme and select SSLE zone. Then, we partitioned the selected zone using a pair of H and α thresholds estimated as follows:

$$H_{\text{th}} = \left[\left(\tilde{H}_{\text{no\_oil}} + \tilde{H}_{\text{oil}}\right) \pm \left|S_{\text{no\_oil}}^{\tilde{H}} - S_{\text{oil}}^{\tilde{H}}\right|\right]\Big/2 \qquad (4)$$

$$\alpha_{\text{th}} = \left[\left(\tilde{\alpha}_{\text{no\_oil}} + \tilde{\alpha}_{\text{oil}}\right) \pm \left|S_{\text{no\_oil}}^{\tilde{\alpha}} - S_{\text{oil}}^{\tilde{\alpha}}\right|\right]\Big/2 \qquad (5)$$

where $\tilde{H}$ and $\tilde{\alpha}$ are the average values of H and α, respectively, and S is the standard deviation. The subscripts "no_oil" and "oil" denote the H and α parameters derived from the uncontaminated and oil-contaminated ice regimes. It should be noted that descriptive statistics (specifically, the average and standard deviation values) play an important role in estimating this pair of thresholds. Only those clusters within the SSLE zone are considered to be eligible for the threshold boundary decision. In the event of an oil spill, any cluster above the threshold pair is labeled as "oil-contaminated ice;" otherwise, it is labeled as "oil-free ice."

To implement this classifier on our scatterometer (coherency matrix) datasets, we trained the algorithm on the phase-1 oil tub because they contain backscattering responses from both oil-free and oil-contaminated ice regimes. Regimes II and III
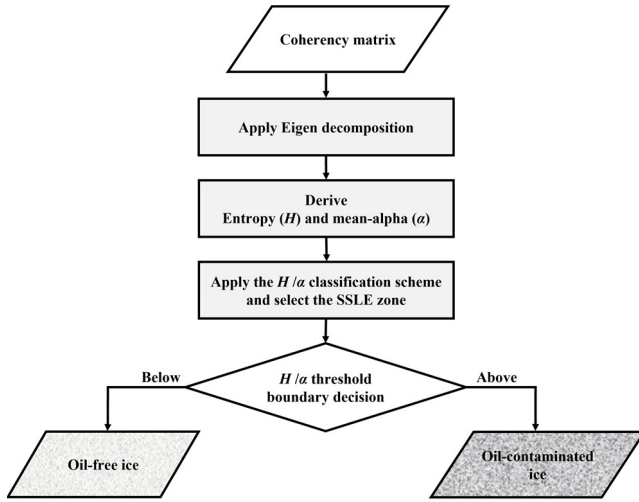
Fig. 2. Threshold classifier algorithm used to discriminate between oil-contaminated and oil-free sea ice in the SSLE zone of entropy/mean-alpha classification plane. SSLE refers to "surface scattering low entropy."

were merged to group oil-free ice and regimes IV and V were merged to group oil-contaminated ice, based on the NRCS sensitivity at C-band frequency. Afterward, we tested the threshold classifier on phase-1 control tub and phase-2 oil tub.

Given that the trained and tested datasets were obtained using similar experimental designs over a shorter duration (<2 days), we expanded the classification analysis with a different experimental setup over a longer duration (8 days) to assess the robustness of the proposed classifier. As a result, in February 2021, we embarked on new SERF campaign to collect C-band scatterometer measurements from a growing ice in the main pool. Hereafter, this experiment is referred to as phase-3 experiment. The scatterometer was configured to scan at incidence angles ranging from 25° to 60° (in five steps). We collected 775 scatterometer samples and considered 39 independent samples (at 30° incidence angle) during the spatial averaging process. Throughout the experiment, under cold temperature (<-25 °C), the ice grew (38 cm thick) in the absence of oil contamination, with frost flowers covering the surface.

III. RESULTS

Following the methods in Section II, we present our results into two subsections that correspond to the research questions posed in Section I. First is a time-series response of SPAN, R_{co}, R_{xo}, v, ρ_{co}, and μ parameters to observe their responses when the NI is contaminated with oil. Second is a scatterplot of H and α parameters, where a threshold classifier was applied within the SSLE zone of the H/α classification plane to distinguish between oil-contaminated and uncontaminated ice.

A. Time-Series Response of Polarimetric Parameters

Fig. 3 shows the time-series response of SPAN, R_{co}, R_{xo}, v, ρ_{co}, and μ parameters for phase-1 and phase-2 experiments (see Section II-A for the description of each experimental phases).

1) Total Power (SPAN): The SPAN values were relatively constant across all phases, averaging 2.5 dB. However, in phase-1 oil tub, we noticed minor deviations from the mean value between 4 and 6 h (1.5 dB decrease), 22 and 32 h (2.5 dB increase), and 32 and 36 h (0.5 dB decrease).

2) Copolarization Ratio (R_{co}) and Cross-Polarization Ratio (R_{xo}): R_{co} and R_{xo} displayed highly variable characteristics, with upward and downward trends throughout the experiment [see Fig. 3(a), left]. When a short-lived frost flower covers the ice surface at 6 h, we observed a continuous transient maximum (20 dB increase) and minimum (10 dB decrease) for R_{co}, as well as a coincidental minimum (10 dB decrease) for R_{xo} immediately after the ice transitioned from Regime-I to Regime-II (refer to Section II-B4 for ice regime definitions). Following the ice transition and oil injection, the R_{co}-parameter monotonically decreased between 13 and 22 h and then was accompanied by a weak oscillation in Regime-IV. Conversely, the R_{xo}-parameter monotonically decreased over the same time range, followed by a local maximum (12 dB increase) in the same ice regime. Prior to oil migration on the ice surface between 31 and 34.5 h, R_{co} gradually increased by 2 dB and then abruptly decreased by 7 dB, whereas R_{xo} responded with a strong minimum (18 dB decrease). Once the oil migrated on the ice surface at 34.5 h, both R_{co} and R_{xo} values strictly trended upward.

In phase-1 control tub, the R_{co}-parameter began with a slow upward trend from 0 to 2 dB for 2 h and remained relatively constant until 32 h (within Regime-IV + V), when it gradually trended downward to -2 dB [see Fig. 3(a), left]. The R_{xo}-parameter, on the other hand, had a monotonic downward trend until 32 h, when it became highly variable and trended in a sinusoidal fashion.

With regard to phase-2 oil tub, the parameters (R_{co} and R_{xo}) remained relatively constant throughout the experiment at approximately 3 and -4 dB, respectively [see Fig. 3(a), right].

3) Geometric Intensity (v): The v-parameter followed the same trend as the R_{xo}-parameter. For example, we observed that the v-parameter experiment, as well as the presence of two local minima—the first when the ice transitioned into Regime-II and the second when the ice transitioned into Regime-V. Prior to the oil migration, similar local maximum was observed within Regime-IV. Our analysis of Pearson's correlation between the v- and R_{xo} values revealed a strong positive relationship (i.e., correlation coefficient >0.75 at 0.0001 significance level). The only difference between the v- and R_{xo}-parameters is that the v-parameter has a lower magnitude response than the R_{xo}-parameter. As such, we will exclude the v-parameter from the discussion section to avoid redundancy.

4) Copolarization Correlation Coefficient (ρ_{co}) and Conformity Coefficient (μ): The ρ_{co} values were highly variable from the start of the phase-1 oil tub experiment, rising sharply from 0.40 to 0.90 as the ice transitioned from Regime-I to Regime-II, and then dropping to 0.65 at about 8 h [see Fig. 3(b), left]. Following the oil injection beneath the ice, the ρ_{co}-parameter increased from 0.8 to 0.95 between 13 and 22 h; however, as the ice changed from Regime-III to Regime-IV, it decreased
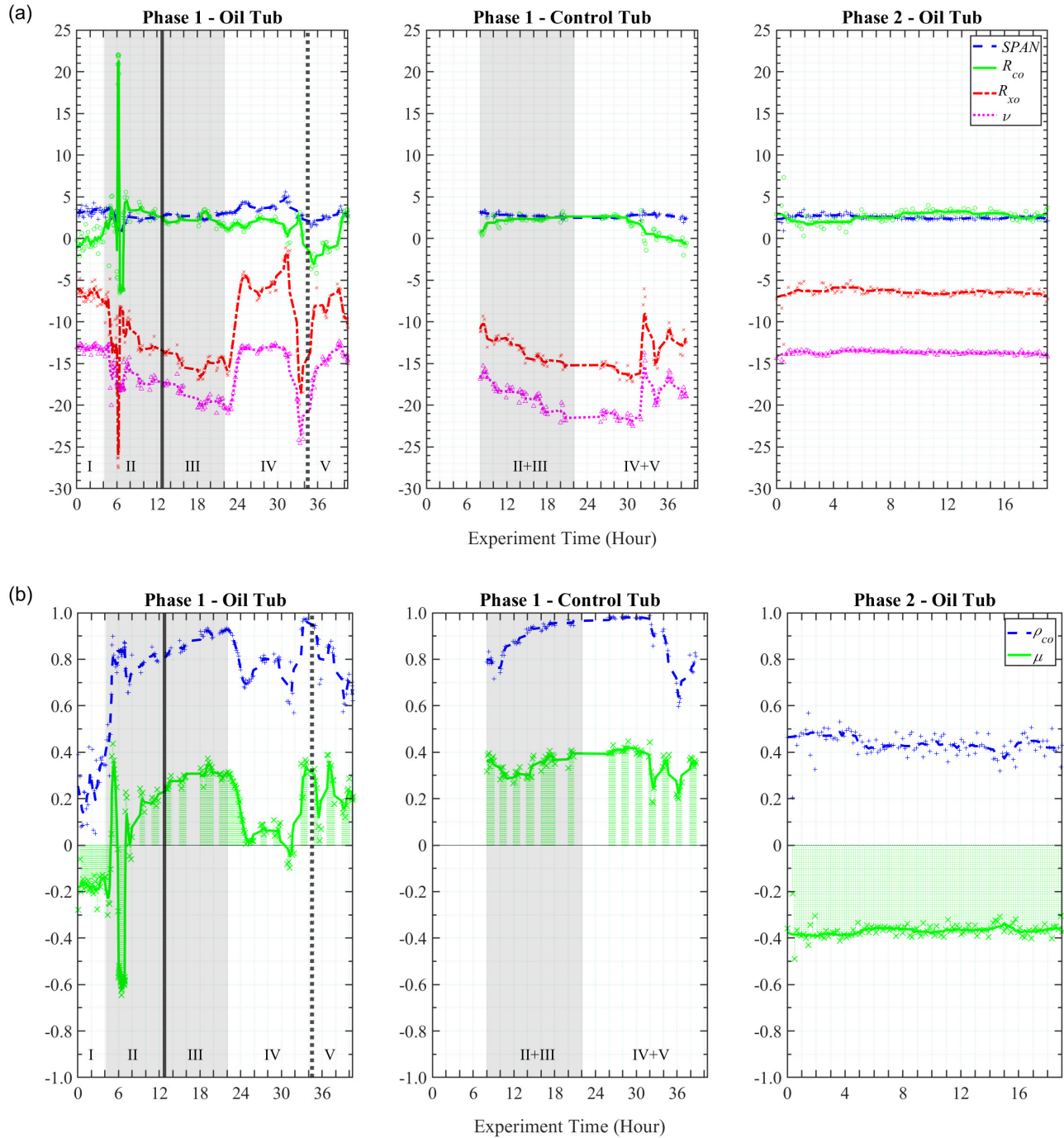
Fig. 3. Time-series response of polarimetric parameters for phases 1 and 2 experiments. (a) Total power (SPAN), copolarization ratio (R_{co}), cross-polarization ratio (R_{xo}), and geometric intensity (ν). (b) Copolarization correlation coefficient (ρ_{co}) and conformity coefficient (μ). The ice regimes definitions (in phase-1 oil tub: I–V; and in phase-1 control: II + III and IV + V) are explained in Table I. Note that the incidence angle is 24.5°, except for the phase-1 control tub which is 22.5°. In the top panel (left), the observed R_{co} and R_{xo} spikes at 6 h represent a short-lived frost flower growth Similarly, in the bottom panel (left), the μ-parameter displayed transitory upward and downward spikes between 4 and 6 h, which represent a period of rapid ice growth and short-lived frost flower growth, respectively (see more details in Section IV-A1).

to 0.7 at 24 h, with a minor uplift between 24 and 31 h. Close to 32 h, the ρ_{co}-parameter trended upward from 0.60 to 0.98, but once the oil migrated onto the ice surface in Regime-V, the trend reverted back to 0.60. Considering the μ-parameter, it remained relatively constant below 0 within the Regime-I. However, as the ice grew into dark nilas (Regime-II) and was sparsely cover with a short-lived frost flower between 4 and 6 h, we observed a transitory behavior in which the

μ values oscillated above and below zero. Following the oil injection, the μ-parameter exhibited similar behavior to that of ρ_{co}-parameter (e.g., first, the μ-parameter trended upward from 0.2 to 0.4 between 13 and 22 h; second, as the ice transitioned from Regime-III to Regime-IV, it abruptly decreased to 0 at 24 h, followed with a minor uplift between 24 and 31 h; and third, it increased from −0.1 to 0.4 close to 32 h). When the oil migrated onto the ice surface, the μ-parameter

depicted a variable characteristics with values greater than zero.

In phase-1 control tub, the ρ_{co}-parameter gradually decreased from 0.80 to 0.70 within Regime-II + III, and then gradually increased from 0.70 to 0.95 between 10 and 22 h. From 32 h, the ρ_{co} values slightly dropped from 0.95 to 0.80 until rapidly reverting to an upward trend direction [see Fig. 3(b), left]. Meanwhile, the μ-parameter began with a slight decrease from 0.4 to 0.3 in Regime-II + III and then gradually increased to 0.4 between 10 and 22 h. In Regime-IV + V, it remained relatively constant at 0.4 until 32 h when the μ-parameter exhibited an oscillatory behavior.

Regarding the phase-2 oil tub, throughout the experiment, both parameters (ρ_{co} and μ) were relatively stable at 0.45 and −0.4, respectively [see Fig. 3(b), right].

B. Entropy/Mean-Alpha Classification and Threshold Classifier

The scatterplots of entropy (H) versus mean-alpha (α) for phases 1 and 2 experiments are shown in Fig. 4. Notably, the H and α parameters were calculated from the eigen decomposition of the coherency matrix, where the former and latter are directly related to the eigenvalues and eigenvectors, respectively (refer to Section II-C).

Fig. 4(a) shows that almost all of the measurements in each of the ice regimes (hereafter referred to as clusters) were enclosed in the SSLE zone of the H/α classification plane. There are few exceptions that occur on and outside the boundary, but the mean value generally lies within the SSLE zone (see Table III). As such, only the oil tub samples from phases 1 and 2 were reduced by 13% (from 201 to 174) and 3% (from 123 to 119), respectively. We observed that the oil-free clusters in phase-1 oil tub (Regimes II and III) and control tub (Regimes II + III and IV + V) are mostly located between 0.1 and 0.3 along the entropy axis and below 18° along the mean-alpha axis. Note that the only exception is Regime-I of phase-1 oil tub, which exhibit high variability, resulting in some measurement points falling within the medium entropy zones. Meanwhile, the oil-contaminated clusters in phase-1 oil tub (Regimes IV and V) were highly variable and distributed linearly along the SSLE zone from the lower left corner to upper right corner. In the phase-2 experiment, the oil-contaminated clusters are found above 0.3 along the entropy axis and above 18° along the mean-alpha axis. Moreover, the variability of these clusters is lower than that of the phase-1 experiment.

Fig. 4(b) illustrates the use of the threshold classifier within the SSLE zone to separate oil-contaminated NI from its oil-free surroundings. The threshold classifier algorithm is explained in Section II-D. Based on the descriptive statistics of phase-1 oil tub, which serve as the training dataset, we calculated the H-parameter to be 0.30 ± 0.02 and the α-parameter to be 19° ± 2° (see Table III). However, with careful visual inspection, we optimally chose our boundary decision on 0.3-H and 18°-α. These boundary decisions were tested on the existing ice regimes in phase-1 control tub and phase-2 oil tub, where clusters above the threshold are labeled "oil-contaminated ice;" otherwise, "oil-free ice." The label accuracy of the ice regimes is summarized in Table IV. As seen in phase-1 oil tub, the true labels for oil-free and oil-contaminated ice were 87% and 57%, respectively. Meanwhile, in the phase-1 control tub, which contains only oil-free ice was 96% correct for Regime-II + III and 92% correct for Regime-IV + V. The true labels for phase-2, in which ice is contaminated with oil, are 100%.

The threshold levels and approach were developed and demonstrated using data from our SERF 2020 experiment. To test the approach on a completely unique dataset, we applied the thresholding approach to the measurements from our SERF 2021 experiment. We knew in advance that there was no oil present, so the algorithm was expected to show that all of the clusters would fall below our boundary decision. Fig. 5 shows the results and clearly demonstrates the robustness of the threshold classifier using the phase-3 scatterometer dataset acquired from the experimental pool. The classification correctly identifies the sea ice as oil-free with 100% accuracy.

IV. DISCUSSION

The goal of this study was to evaluate the potential of C-band polarimetric parameters for discriminating oil spills on NI based on the backscatter mechanisms associated with changes in geophysical and thermodynamics states. This section discusses the interpretations based on the two sets of results presented in Section III. To begin, we perform a sensitivity analysis on the temporal evolution of polarimetric parameters to ascertain which parameterization best responds to oil-contaminated NI. Following that, we conduct a separation analysis using the H/α classification plane to isolate oil-contaminated NI from its oil-free ice surroundings.

A. Sensitivity Analysis

Sensitivity analysis provides a premise for understanding the responsiveness of polarimetric parameters to changes in different sea ice scattering mechanisms and will be employed to answer our first posed research question in Section I, "which time-series responses of SPAN, R_{co}, R_{xo}, ρ_{co}, μ, and ν of NI are the most sensitive to an oil within or on ice spill event?" The time-series response of polarimetric parameters in Fig. 3 revealed the sensitivity toward the contributions from both surface and volume scattering mechanisms.

1) Phase-1 Oil Tub Experiment: In the phase-1 oil tub, the ice grew from calm open water through frazil. When the ice became dark nilas, oil was injected beneath the ice. The dark nilas developed into light nilas and the oil eventually migrated through it and onto the ice surface. Throughout the experiment, the *SPAN* parameter remained relatively constant with some minor deviations at particular time intervals [see Fig. 3(a), left]. This constant behavior suggests that the SPAN parameter is insensitive to the growth of NI, whereas the small anomalous deviations indicate an extremely weak sensitivity to changes in scattering mechanisms that are the functions of surface brine expulsion (between 4 and 6 h), oil encapsulation (between 22 and 32 h), and surface oil migration (between 32 and 36 h).
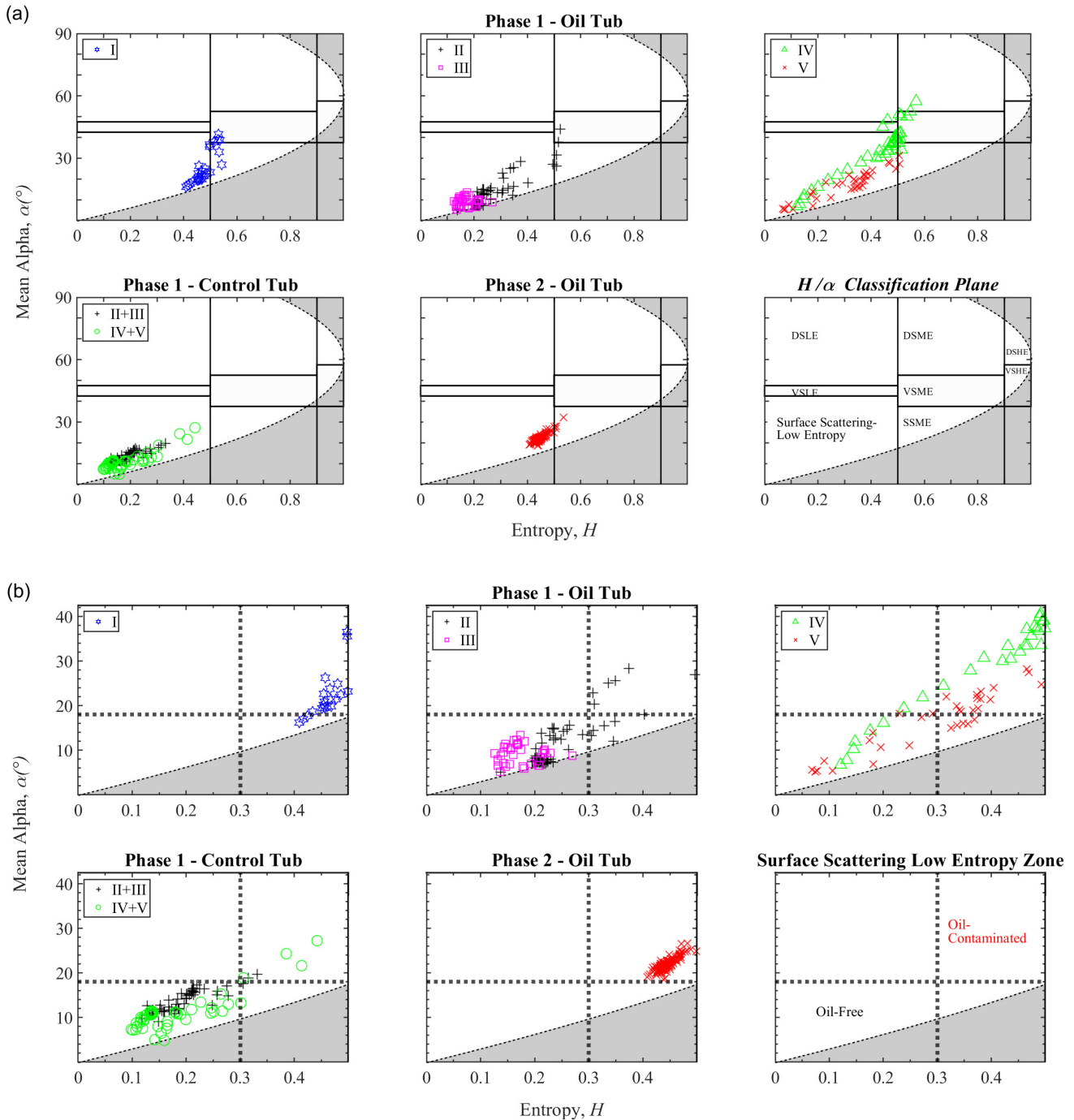
Fig. 4. Scatterplot of entropy (H) versus mean-alpha (α) for phases 1 and 2 experiments. (a) H/α classification plane for ice regimes. (b) SSLE zone within the H/α classification plane. The vertical and horizontal dotted lines represent the set of threshold of 0.3-H and 18°-α used to segment oil-contaminated ice from oil-free ice. The ice regimes definitions (in phase-1 oil tub: I–V; and in phase-1 control: II + III and IV + V) are explained in Table I. Note that the incidence angle is 24.5°, except for the phase-1 control tub, which is 22.5°.

This is the first time, to the best of our knowledge, that this result has been observed for oil-contaminated sea ice, so additional time-series data are required for confirmation.

The R_{co} and R_{xo} parameters were highly variable, minimizing, and maximizing changes in physical scattering processes. Although the R_{co}-parameter exhibited a local minimum due to the complex physical processes involved in rapid ice growth, its trend was dominated by two maxima similar to the local scattering peaks observed in the copolarized NRCS (see Fig. 1, left). The first maximum can be related to rapid surface brine expulsion [55], which triggered a short-lived frost flower growth at 6 h [see Fig. 4(a), left]. This short-lived growth was due to a shallow temperature gradient between the ice surface and its near-surface atmosphere [31]. The second maximum can be related to a combination of upward brine expulsion and oil migration [31]. This suggests that R_{co} is sensitive to changes in surface scattering. In contrast, the trend of the R_{xo}-parameter was dominated by

TABLE III
STATISTICS OF ENTROPY (H) AND MEAN-ALPHA (α) PARAMETERS WITHIN THE SSLE ZONE FOR PHASES 1 AND 2 EXPERIMENTS

	Ice Regime	n	$\widetilde{H}$	$S^{\widetilde{H}}$	$\tilde{\alpha}$	$S^{\tilde{\alpha}}$
Phase-1 oil tub	I	20	0.46	0.03	22.39	5.33
	[II–III]*	93	0.22	0.06	10.69	4.75
	[IV–V]*	61	0.33	0.13	22.12	10.46
Phase-1 control tub	II+III	50	0.25	0.04	10.96	3.11
	IV+V	48	0.14	0.03	9.65	3.98
Phase-2 oil tub	IV+V†	119	0.45	0.02	22.02	1.56

SSLE zone represents the zone of surface scattering low entropy zone of the entropy/mean-alpha classification plane. n = number of samples, $\widetilde{H}$ = average value of H, $\tilde{\alpha}$ = average value of α, S = standard deviation. In phase-1 oil tub, Regime-I, Regime-[II–III]*, and Regime-[IV–V]* represent open-water/frazil, oil-free dark nilas, and oil-contaminated light nilas, respectively. The superscripts * indicate that Regimes II and III were merged to form Regime-[II–III] and Regimes IV and V to form Regime-[IV–V], based on their C-band NRCS sensitivity to oil spill. Meanwhile, in phase-1 control tub, Regime-II+III represents oil-free dark nilas, whereas Regime-IV+V represents oil-free light nilas. For phase-2 oil tub, Regime-IV+V† represents oil-contaminated light nilas.

TABLE IV
THRESHOLD CLASSIFIER USING 0.3-ENTROPY AND 18°-MEAN-ALPHA

	Ice Regime	n	Classifier	TRUE	Comment
Phase-1 oil tub	I	20	Open water/frazil	0	Training dataset
	[II–III]*	93	Oil-free ice	87%	
	[IV–V]*	61	Oil-contaminated ice	57%	
Phase-1 control tub	II+III	50	Oil-free ice	96%	Testing dataset
	IV+V	48	Oil-free ice	92%	
Phase-2 oil tub	IV+V†	119	Oil-contaminated ice	100%	
Phase-3 pool	IV+V**	775	Oil-free ice	100%	

Except for the phase-3 oil-free pool, where Regime-IV+V** represents oil-free light nilas and beyond, the other ice regime definitions can be found in Table III.
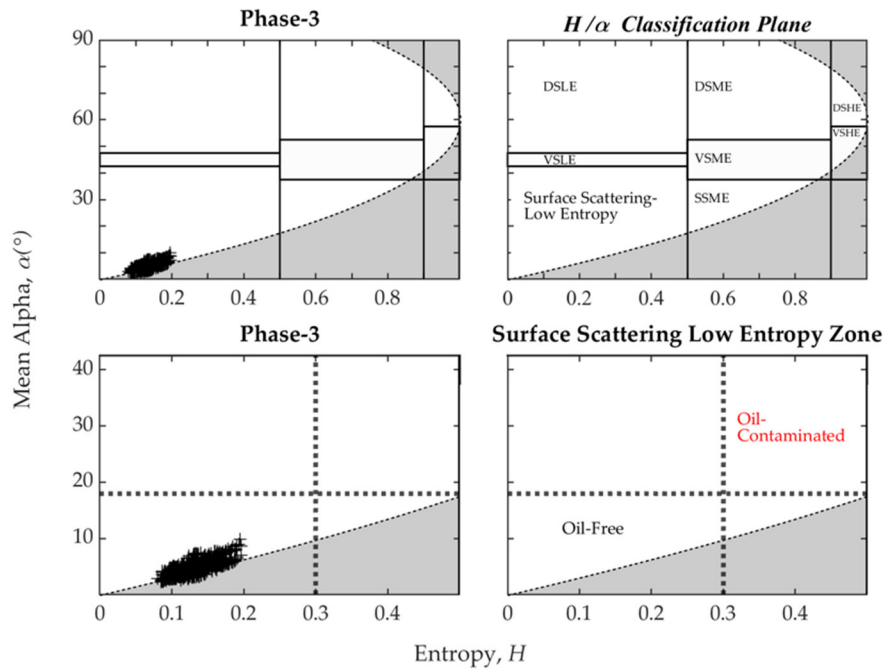

Fig. 5. Scatterplot of entropy (H) versus mean-alpha (α) for phase-3 uncontaminated pool experiment at an incidence angle of 30°.

two local minima and one local maximum. With the exception of the first minimum, the remaining minimum and maximum values were consistent with the scattering spikes observed in the cross-polarized NRCS (see Fig. 1, left). As such, we associated the first minimum to a depolarization effect from the rearrangement of brine pockets during rapid ice growth [16]. There is a lack of detailed microstructural analysis of the

depolarization effect during initial ice formation, making the interpretation difficult and necessitating further investigation. Meanwhile, the second minimum was linked to an upward oil migration caused by increasing ambient temperatures approaching the freezing point [31, Fig. 4]. Prior to the oil migration, the only maximum within Regime-IV indicates a heterogeneous NI layer, which Asihene et al. [31] attributed

to volume scattering caused by the oil encapsulation within the ice medium.

Regarding the ρ_{co}-parameter, its trend in Fig. 3(b) (left) followed a similar scattering pattern to the copolarized NRCS in Fig. 1 (left), indicating that this parameter was susceptible to changes in both surface and volume scatterings. In response to the changes in surface scattering: first, the ρ_{co} values strictly increased during the growth of frost flowers; second, it exhibited a rapidly increasing trend during the ice thickening; and third, it decreased when oil migrated and wetted the ice surface. In response to changes in volume scattering, the ρ_{co} values decreased when oil migrated and became encapsulated, thereby introducing inhomogeneity within the ice [31]. We observed that this parameter de-emphasized oil encapsulation, which is opposite to the response observed in the R_{xo}-parameter. This decrease occurs because the ρ_{co}-parameter is expected to suppress decorrelation from cross-polarized scattering responses within the ice volume. In comparison to a previous study, Nghiem et al. [17, Fig. 18(b)] reported the ρ_{co} value to be 0.50 at 25° incidence angle, where the ice thickness was <4 cm. This value was less than what we observed, which was 0.80 at 24.5° incidence angle, where the ice thickness was 3.4 cm at 8 h [31, pp. 5]. Our higher value was due to the presence of frost flowers, which enhance the surface dielectrics; however, the enhancement was not prominent due to the sparse distribution of frost flowers on the ice surface [31, Fig. 3(c)]. Therefore, a wide distribution of frost flower growth is required to be discernible using the ρ_{co}-parameter.

As shown in Fig. 3(b) (left), the μ-parameter demonstrated a logical trend that characterized the ice regimes into slightly rough (Bragg) and specular (non-Bragg) types of surface scattering behavior. This trend was evident in a study of mapping ocean surface oil slicks conducted by Zhang et al. [12]. They found that Bragg scattering is linked to oil-free water and non-Bragg scattering to oil-slick water. In our case, we attributed the Bragg scattering to the highly saline nature within the topmost layer of the NI surface (or its near surface) and the non-Bragg scattering to the oil dampening effect on the ice surface. Within Regime-II (i.e., dark nilas), the unexpected behavior of negative μ values at 6 h was caused by a short-lived frost flower cover that formed after the rapid ice growth in 4 h. We attributed the short-lived growth event to a weak temperature gradient between ice surface and its relative near-surface atmosphere [31]. Prior to the oil migration, the μ values were positive and close to the zero-level, indicating that it was sensitive to the changes in volume scattering as the oil became encapsulated within the ice. We observed similar behavior with the ρ_{co}-parameter, implying that both the μ and ρ_{co} parameters are related in terms of being sensitive to oil encapsulation within the ice. When the oil became visible on the ice surface, the μ values remained positive. This is in contrast to the findings of Zhang et al. [12], where a high volume of oil slick on the ocean surface were detected with negative μ values. We speculate that the low fractional oil volume (0.7%) was the reason that the μ-parameter did not indicate the presence of the oil [31], but when compared to phase-2 oil tub in Fig. 3(b) (right), the

fractional oil volume (3%) was much higher [31], resulting in the expected negative μ values. This means that a greater volume of oil is required for the μ-parameter to be sensitive to oil spill on ice.

2) Phase-1 Control Tub Experiment: Nilas ice was grown in oil-free seawater in the phase-1 control tub. As shown in Fig. 3(a) (middle), the SPAN was strictly constant throughout the experiment and is in agreement with the phase-1 oil tub, especially when no oil has been injected beneath the ice. This means that it lacks sensitivity to changes in surface scattering as the ice grows. Previous studies by Isrealsson and Askne [43, Fig. 2(b)] found that SPAN values were constant at different incidence angles within the C-band frequency, whereas we observed the temporal variation at a single incidence angle (22.5°). Despite this lack of responsiveness, the relative temporal consistency of the SPAN values may be useful for evaluating the quality assurance and quality control of NI scatterometer measurements at C-band; however, this requires further investigation.

The R_{co}-parameter depicted a gradual upward trend within Regime-II + III, and when compared to the phase-1 oil tub, a similar pattern was observed, albeit with a monotonic behavior. This demonstrates a low response to changes in surface scattering as the dark nilas thickens. Because this parameter increases with increasing incidence angle [8], [9], we anticipate it to be more responsive as the ice grows at higher incidence angles (>35°). In contrast, R_{xo} maintained a steady downward trend, which was expected given that both parameters are more sensitive to volume scattering (as discussed in Section IV-A1). As the ice transitioned from Regime-II + III to Regime-IV + V, these parameters (R_{co} and R_{xo}) were relatively constant, indicating a period during which the ice developed from dark nilas to light nilas. From 32 h, the R_{co}-parameter gradually trended downward, whereas the R_{co}-parameter fluctuated with momentary spikes. This behavior was not anticipated because R_{co} was expected to increase while R_{xo} is expected to decrease. We attributed this effect to the accumulation of snowfall traces on the ice surface [31, Fig. 3(e)]. Although similar snow traces were visible in the phase-1 oil tub, their effect was minimal when compared to phase-1 control tub. As a result, it is clear that in the absence of snowfall, the R_{co} and R_{xo} parameters are suitable for discriminating between dark nilas and light nilas.

The ρ_{co} values gradually increased within dark nilas, and it approaches one as the ice transitioned into light nilas [see Fig. 3(b), middle]. This means that the ρ_{co}-parameter is sensitive to surface scattering as the ice grows, similar to what we observe in phase-1 oil tub. A study by Isleifson et al. [18] demonstrated that the ρ_{co} parameter is capable of distinguishing NI with ice thicknesses <6.0 and >8.0 cm. At a 25° incidence angle, the average ρ_{co} value for ice thickness <6.0 cm was 0.55, while for ice thickness >8.0 cm was 0.90; they found a resulting difference of 0.35 [18]. In comparison, our values at a 24.5° incidence angle were 0.80 and 0.90 for <6.0 and >8.0 cm ice thicknesses, respectively, resulting in a 0.1 difference. This is within the error bounds shown in [18, Fig. 4]. The highly saline topmost layer of NI contributed to the lower contrast between the two ice regimes in our

study [31]. Similar to the abnormal characteristics observed in R_{co}-parameter from 32 h, the ρ_{co}-parameter changed from the expected upward trend to a downward trend. This is a confirmation that the contribution of snow has altered that ice scattering behavior.

Regarding the time-series response of the μ-parameter [see Fig. 3(b), left], we found a logical trend, in which positive μ values are assigned to both dark nilas (Regime-II + III) and light nilas (Regime-IV + V). This logical trend was consistent when compared to the phase-1 oil tub, except during the initial ice growth and when our C-band scatterometer measurement became responsive to the oil within the ice volume. Unlike the ρ_{co}-parameter, the μ-parameter lacks the sensitivity of increasing ice growth because no discernible contrast was seen between the dark nilas and light nilas.

3) Phase-2 Oil Tub Experiment: In the phase-2 oil tub, nilas ice was grown in oil-contaminated seawater. The time-series responses of SPAN, R_{co}, R_{xo}, ρ_{co}, and μ in Fig. 3 (right) showed relatively stable characteristics that were consistent with all of the polarimetric NRCS in Fig. 1 (right), indicating specular scattering behaviors. This specular scattering is caused by an oil layer on the ice surface, which obscures NRCS detection of the ice growth beneath, potentially posing a safety risk to vessel navigation [31]. In terms of SPAN, its scattering behavior is steady and consistent with that of the phase-1 control, implying that this parameter is less informative at C-band for oil spill detection.

With the exception of the SPAN and R_{co} parameters, other polarimetric parameters exhibited a substantial contrast from those in phase-1 control tub. Furthermore, these other parameters displayed no trending patterns compared to trending patterns in phase-1 control tub (decreasing trends for R_{xo} and variable trends for ρ_{co} and μ). This implies that the R_{xo}, ρ_{co}, and μ parameters are sensitive to the scattering contributions of when NI is oil-free and oil-contaminated. In particular, the μ-parameter would be effective for discriminating between uncontaminated and oil-contaminated light nilas because the former is explicitly discernable by negative μ values and the latter by positive μ values [see Fig. 3(b), left and right].

B. Separation Analysis

To answer the second research question in Section I, "is it possible to effectively separate oil-contaminated NI from oil-free NI by using the relationship between H and α parameters?" we used these parameters to establish a classification scheme that delineates the scattering contributions of our experimental ice regimes as SSLE zone. Within this zone, we developed a threshold classifier to discriminate between oil-contaminated and oil-free NI (see Figs. 4 and 5). Phase-1 oil experiment was used to train the threshold algorithm, while phase-1 control tub, phase-2 oil tub, and phase-3 oil-free pool were used to validate the results.

With the exception of a few cluster points (which represents the ice regimes), we observed that almost all of the ice regimes in Fig. 4(a) resulted in similar dominant scattering behavior as they clustered within the SSLE zone. This clustering is

expected because homogenous-level sea ice is modeled as surface Bragg scatterer, which strongly contributes to SSLE classification [33]. Even when oil masked the ice surface, during phase-1 oil tub (Regime-V) and phase-2 oil tub, the dominant specular surface scattering mechanism was still within the SSLE region. This is because the presence of oil smoothens the ice surface, which in turn acts a specular reflector to the incoming radar signals. In phase-1 oil tub [see Fig. 4(a), upper panel], those few clusters outside the SSLE region were associated with high depolarization effect that occurred during the upward brine expulsion as the ice rapidly transitioned from Regime-I to Regime-II, as well as oil encapsulation within Regime-IV. When all the cluster points within the SSLE zone were considered, the H versus α scatterplot revealed how highly variable the backscattering response of NI is [see Fig. 4(b)]. This high variability appeared to reveal a decision boundary, in which Regime-I was distributed on the extreme middle right, Regimes II and III were distributed around the bottom left, and Regimes IV and V were linearly distributed from the bottom left to the upper right.

Visual inspection, analysis, and interpretations are the common approaches used by sea ice analysts (e.g., see [49], [53], [54], [56]). Given the high variable nature of sea ice physical properties, a sea ice expert can incorporate a priori information from ambient environments, as well as other events such as oil spills, to determine the optimal set of thresholds that imposes a suitable boundary on the actual data at hand [53]. For example, as shown in Table III, the statistics of both the oil-free and oil-contaminated NI were almost differentiated by values above and below the optimized threshold pair (0.3-H and 18°-α). Although, this is the first time an oil-in-ice experiment involving the H and α parameters has been performed, our average values for the uncontaminated and oil-contaminated NI were consistent with those reported by Johansson et al. [9, pp. 4] at lower incidence angles.

The label accuracy of the H/α threshold classifier on phase-1 oil tub, phase-1 control tub, phase-2 oil tub, and phase-3 oil-free pool was shown in Table IV. A complete false label was achieved for Regime-I (open water/frazil), as expected, because the backscattering response had been affected by noise equivalent sigma zero (NESZ), which is the receiver noise floor in our scatterometer system. The estimated average NESZ in this study was -45 dBm^2/m^2 for the copolarized NRCS and -50 dBm^2/m^2 for cross-polarized NRCS [31]. When compared to the magnitude of NRCS in Regime-I (Fig. 1, left), the copolarized NRCS was on average -43.5 dB, whereas the cross-polarized NRCS was relatively at -50 dB, indicating that the NRCS was essentially at the instrument noise floor. These noise-affected H and α values were presented to illustrate the usefulness of NESZ estimation for quality assurance and quality control purposes during separation analysis (e.g., see [57]). Another reason for the completely false label is that the H/α threshold classifier method is not applicable when ice thickness is less than 2 cm, and further investigation is required for this specific situation.

Based on C-band NRCS sensitivity to oil spill in phase-1 oil tub (see Section II-D), Regimes II and III were combined to form Regime-[II–III]∗ (oil-free dark nilas) and Regimes IV and V were combined to form Regime-[IV–V]∗ (oil-contaminated light nilas). As shown in Table IV, our proposed threshold classifier successfully distinguished between oil-free and oil-contaminated ice in both the training and testing datasets. We attributed all misclassifications of the oil-free NI to transitional growth between ice regimes, as well as snowfall accumulation. This snow accumulation is the same reason we observed unexpected sensitivities from 32 h in the time-series response of phase-1 control tub's NRCS (see Fig. 1) and polarimetric parameters (except SPAN, see Fig. 3). For the oil-contaminated NI, we attributed all misclassifications to oil migrating upward toward the ice surface. These findings suggest that the H and α relationship could be used to detect oil in ice-laden waters at a C-band radar frequency, especially when the oil forms a skim layer on the ice surface.

The separation analysis clearly demonstrated that our proposed H/α threshold classifier possesses enormous potential for discrimination of oil spill in ice-laden waters; however, the small sample size and similarities of phases 1 and 2 experiments initiated further investigation. This is why phase-3 dataset was included, as its sample size ($n = 775$) is significantly larger than that of the previous phases (see Table IV) and was collected using a different experimental setup (see Sections II-A and II-D). Fig. 5 revealed that all the phase-3 clusters fall below the boundary decision, indicating that the ice regime was oil-free. This result is unique because it validates the robustness of our threshold classifier and also illustrates that its performance is not constrained by sample size. Future work will include investigating the thresholding algorithm approach to other oil spill and nonoil spill remote sensing data, such as those we plan to conduct at the Churchill Marine Observatory [58].

V. Conclusion

This manuscript has presented an analysis of C-band polarimetric parameters extracted from the normalized radar cross section, covariance matrix, and coherency matrix of oil-free and oil-contaminated NI. The derived eight polarimetric parameters include SPAN, R_{co}, R_{xo}, ν, ρ_{co}, μ, H, and α. We related all these parameters to backscatter mechanisms associated with changes in thermophysical properties, using the ice cores sampled during two phases of oil-in-sea ice mesocosms: 1) oil was injected beneath an established ice and 2) ice was grown in an oil-contaminated artificial seawater.

Results from the time-series responses of SPAN, R_{co}, R_{xo}, ν, ρ_{co}, and μ were observed to determine which one was respond best in the aftermath of an oil spill (see Fig. 3). We found that the ρ_{co}-parameter is the most reliable polarimetric parameter in an oil spill detection because it provides information on both surface and volume scattering, which are related to various oil spill scenarios, including oil encapsulated within ice and oil spreading on the ice. Meanwhile, we found that the SPAN parameter is the least reliable parameter for

temporal discrimination between oil-contaminated NI and its oil-free surroundings; however, we recommend it for data quality control purposes. Other parameters, such as R_{co}, can be used as an auxiliary to diagnose the changes in surface scattering mechanisms, whereas R_{xo} and ν are useful for responding to changes in volume scattering. Because R_{xo} and ν parameters have similar sensitivity behavior, only one should be employed to avoid redundancy. We recommend the R_{xo}-parameter because it is less computationally demanding and less susceptible to the scatterometer noise floor. One unique observation about the μ-parameter is that it can differentiate between oil-contaminated ice (with negative μ values) and the oil-free ice (with positive μ values). This is feasible if the amount of oil spill volume is large enough and the ice thickness is ≥ 5 cm. Overall, no single polarimetric parameters should be used in isolation, particularly in an oil spill event where we want to eliminate oil-lookalikes to accurately detect and monitor oil within and on the ice.

We investigated the possibility of distinguishing oil-contaminated and oil-free NI using the H/α classification plane (see Fig. 4). Results showed that both NI with and without oil inclusion will usually fall within the SSLE zone. This zone revealed segmented distributions for different ice regimes, so we developed a threshold classifier for discrimination (see Section II-D). Using the phase-1 oil experiment as a training dataset, we found that a threshold pair of 0.3-H and 18°-α truly labeled 87% of oil-free ice and 57% of oil-contaminated ice (see Table IV). When tested on dataset with phase-1 oil-free experiment and phase 2 oil experiment, we obtained >90% and 100% accuracy, respectively. Misclassifications were attributed to transitional growth between ice regimes, snowfall accumulations, and upward oil migration. Later, we extended our validation with a different experimental design, where ice was grown without oil-contamination (phase-3), and the data collected was much larger than in previous phases. The threshold classifier correctly classified the phase-3 data as oil-free ice (see Fig. 5), demonstrating its robustness and performance with a larger sample size (see Table IV). The significance of this separation analysis is that, despite the high degree of variability in NI physical properties, it is possible to develop a simple and adaptive threshold classifiers within the H/α plane that accurately discriminate between oil-contaminated and oil-free NI.

This study has improved our capability for discriminating oil-contaminated NI from uncontaminated NI. The combination of polarimetric parameters can serve as a complimentary data interpretation for oil detection in the Arctic Ocean using current and future C-band polarimetric radar satellites. The findings of this study are limited to low incidence angles, absence of snowfall, calm conditions, and cold temperatures. Future work will consider analyzing polarimetric parameters with higher incidence angles ($>35°$), as well as longer wavelength such as L-band. To improve the interpretation of the polarimetric parameter results, this study should be extended to a large field scale in the Arctic, where we can collect well-representative meteorological variables, in situ physical ice samples, and sea ice backscatter response;

Canada's Churchill Marine Observatory facility has been proposed to accomplish this in [58].

References

[1] B. Ellis and L. Brigham. (2009). *Arctic Marine Shipping Assessment Report*. Accessed: Dec. 30, 2021. [Online]. Available: http://hdl.handle.net/11374/54

[2] J. Dawson, L. Pizzolato, S. E. L. Howell, L. Copland, and M. E. Johnston, "Temporal and spatial patterns of ship traffic in the Canadian Arctic from 1990 to 2015," *Arctic*, vol. 71, no. 1, pp. 15–26, 2018, doi: 10.14430/arctic4698.

[3] A. K. Y. Ng, J. Andrews, D. Babb, Y. Lin, and A. Becker, "Implications of climate change for shipping: Opening the Arctic seas," *WIREs Climate Change*, vol. 9, no. 2, Mar. 2018, Art. no. e507, doi: 10.1002/wcc.507.

[4] B. M. Boylan and D. Elsberry. (2019). Climate change and maritime traffic in the Arctic. The Center for Arctic Policy Studies. Accessed: Oct. 2, 2021. [Online]. Available: https://uaf.edu/caps/our-work/policy-perspectives-files/climate-change-and-maritime-traffic-in-the-arctic-pb4-final-12dec2019.pdf

[5] A. H. S. Solberg, "Remote sensing of ocean oil-spill pollution," *Proc. IEEE*, vol. 100, no. 10, pp. 2931–2945, Oct. 2012, doi: 10.1109/JPROC.2012.2196250.

[6] R. D. Lindsley and D. G. Long, "Mapping surface oil extent from the deepwater horizon oil spill using ASCAT backscatter," *IEEE Trans. Geosci. Remote Sens.*, vol. 50, no. 7, pp. 2534–2541, Jul. 2012, doi: 10.1109/TGRS.2011.2174369.

[7] M. Fingas and C. Brown, "Oil spill remote sensing," in *Encyclopedia of Sustainability Science and Technology*, R. A. Meyers, Ed. New York, NY, USA: Springer, 2018, pp. 1–37.

[8] C. Brekke, B. Holt, C. Jones, and S. Skrunes, "Discrimination of oil spills from newly formed sea ice by synthetic aperture radar," *Remote Sens. Environ.*, vol. 145, pp. 1–14, Apr. 2014, doi: 10.1016/j.rse.2014.01.015.

[9] A. M. Johansson, C. Brekke, and G. Spreen, "Multi-frequency polarimetric SAR signatures of lead sea ice and oil spills," in *Proc. IEEE Int. Geosci. Remote Sens. Symp. (IGARSS)*, Jul. 2017, pp. 1872–1875, doi: 10.1109/IGARSS.2017.8127342.

[10] A. M. Johansson, M. M. Espeseth, C. Brekke, and B. Holt, "Can mineral oil slicks be distinguished from newly formed sea ice using synthetic aperture radar?" *IEEE J. Sel. Topics Appl. Earth Observ. Remote Sens.*, vol. 13, pp. 4996–5010, 2020, doi: 10.1109/JSTARS.2020.3017278.

[11] F. Nunziata, A. Gambardella, and M. Migliaccio, "A unitary Mueller-based view of polarimetric SAR oil slick observation," *Int. J. Remote Sens.*, vol. 33, no. 20, pp. 6403–6425, Oct. 2012, doi: 10.1080/01431161.2012.687474.

[12] B. Zhang, W. Perrie, X. Li, and W. G. Pichel, "Mapping sea surface oil slicks using RADARSAT-2 quad-polarization SAR image," *Geophys. Res. Lett.*, vol. 38, no. 10, May 2011, Art. no. L10602, doi: 10.1029/2011gl047013.

[13] S. Skrunes, C. Brekke, T. Eltoft, and V. Kudryavtsev, "Comparing near-coincident C- and X-band SAR acquisitions of marine oil spills," *IEEE Trans. Geosci. Remote Sens.*, vol. 53, no. 4, pp. 1958–1975, Apr. 2015, doi: 10.1109/TGRS.2014.2351417.

[14] S. Skrunes, C. Brekke, C. E. Jones, and B. Holt, "A multisensor comparison of experimental oil spills in polarimetric SAR for high wind conditions," *IEEE J. Sel. Topics Appl. Earth Observ. Remote Sens.*, vol. 9, no. 11, pp. 4948–4961, Nov. 2016, doi: 10.1109/JSTARS.2016.2565063.

[15] S. Skrunes, C. Brekke, C. E. Jones, M. M. Espeseth, and B. Holt, "Effect of wind direction and incidence angle on polarimetric SAR observations of slicked and unslicked sea surfaces," *Remote Sens. Environ.*, vol. 213, pp. 73–91, Aug. 2018, doi: 10.1016/j.rse.2018.05.001.

[16] M. R. Drinkwater, R. Kwok, E. Rignot, H. Israelsson, R. G. Onstott, and D. P. Winebrenner, "Potential applications of polarimetry to the classification of sea ice," in *Microwave Remote Sensing of Sea Ice*, F. D. Carsey, Ed. Washington, DC, USA: American Geophysical Union, vol. 1992, pp. 419–430.

[17] S. V. Nghiem, R. Kwok, S. H. Yueh, and M. R. Drinkwater, "Polarimetric signatures of sea ice 2. Experimental observations," *J. Geophys. Res.*, vol. 100, no. C7, pp. 13681–13698, 1995, doi: 10.1029/95jc00938.

[18] D. Isleifson, B. Hwang, D. Barber, R. Scharien, and L. Shafai, "C-band polarimetric backscattering signatures of newly formed sea ice during fall freeze-up," *IEEE Trans. Geosci. Remote Sens.*, vol. 48, no. 8, pp. 3256–3267, Aug. 2010, doi: 10.1109/TGRS.2010.2043954.

[19] A. M. Johansson, C. Brekke, G. Spreen, and J. A. King, "X-, C-, and L-band SAR signatures of newly formed sea ice in Arctic leads during winter and spring," *Remote Sens. Environ.*, vol. 204, pp. 162–180, Jan. 2018, doi: 10.1016/j.rse.2017.10.032.

[20] D. Isleifson, R. Galley, N. Firoozy, J. Landy, and D. Barber, "Investigations into frost flower physical characteristics and the C-band scattering response," *Remote Sens.*, vol. 10, no. 7, p. 991, Jun. 2018, doi: 10.3390/rs10070991.

[21] D. Isleifson, A. S. Komarov, D. Desmond, G. Stern, and D. Barber, "Modeling backscatter from oil-contaminated sea ice using a multi-layered scattering model," in *Proc. IEEE Int. Geosci. Remote Sens. Symp. (IGARSS)*, Sep. 2020, pp. 3031–3034, doi: 10.1109/IGARSS39084.2020.9323887.

[22] "The interaction of crude oil with Arctic sea ice—Beaufort sea project," NORCOR Eng. Res. Ltd., Victoria, BC, Canada, Tech. Rep. 27, 1975. Accessed: Dec. 30, 2021. [Online]. Available: https://www.restco.ca/BSPTR/BSP_TR27_NORCOR.pdf

[23] S. Martin, "A field study of brine drainage and oil entrainment in first-year sea ice," *J. Glaciology*, vol. 22, no. 88, pp. 473–502, 1979, doi: 10.3189/s0022143000014477.

[24] M. Oggier, H. Eicken, J. Wilkinson, C. Petrich, and M. O'Sadnick, "Crude oil migration in sea-ice: Laboratory studies of constraints on oil mobilization and seasonal evolution," *Cold Regions Sci. Technol.*, vol. 174, Jun. 2020, Art. no. 102924, doi: 10.1016/j.coldregions.2019.102924.

[25] D. S. Desmond et al., "Oil behavior in sea ice: Changes in chemical composition and resultant effect on sea ice dielectrics," *Mar. Pollut. Bull.*, vol. 142, pp. 216–233, May 2019, doi: 10.1016/j.marpolbul.2019.03.021.

[26] D. Saltymakova et al., "Effect of dissolution, evaporation, and photooxidation on crude oil chemical composition, dielectric properties and its radar signature in the Arctic environment," *Mar. Pollut. Bull.*, vol. 151, Feb. 2020, Art. no. 110629, doi: 10.1016/j.marpolbul.2019.110629.

[27] N. Firoozy et al., "An electromagnetic detection case study on crude oil injection in a young sea ice environment," *IEEE Trans. Geosci. Remote Sens.*, vol. 55, no. 8, pp. 4465–4475, Aug. 2017, doi: 10.1109/TGRS.2017.2692734.

[28] N. Firoozy et al., "A controlled experiment on oil release beneath thin sea ice and its electromagnetic detection," *IEEE Trans. Geosci. Remote Sens.*, vol. 56, no. 8, pp. 4406–4419, Aug. 2018, doi: 10.1109/TGRS.2018.2818717.

[29] T. D. Neusitzer et al., "Examining the impact of a crude oil spill on the permittivity profile and normalized radar cross section of young sea ice," *IEEE Trans. Geosci. Remote Sens.*, vol. 56, no. 2, pp. 921–936, Feb. 2018, doi: 10.1109/TGRS.2017.2756843.

[30] E. Asihene et al., "C-band backscatter of oil-polluted new sea ice in a mesocosm," in *Proc. IEEE 19th Int. Symp. Antenna Technol. Appl. Electromagn. (ANTEM)*, Aug. 2021, pp. 1–2, doi: 10.1109/ANTEM51107.2021.9518483.

[31] E. Asihene et al., "Toward the detection of oil spills in newly formed sea ice using c-band multipolarization radar," *IEEE Trans. Geosci. Remote Sens.*, vol. 60, pp. 1–15, 2022, doi: 10.1109/TGRS.2021.3123908.

[32] J. Sen Lee and E. Pottier, *Polarimetric Radar Imaging: From Basics to Applications*, 1st ed. Boca Raton, FL, USA: CRC Press, 2009.

[33] S. R. Cloude and E. Pottier, "An entropy based classification scheme for land applications of polarimetric SAR," *IEEE Trans. Geosci. Remote Sens.*, vol. 35, no. 1, pp. 68–78, Jan. 1997, doi: 10.1109/36.551935.

[34] J. Wilkinson et al., "Oil spill response capabilities and technologies for ice-covered Arctic marine waters: A review of recent developments and established practices," *Ambio*, vol. 46, pp. 423–441, Dec. 2017, doi: 10.1007/s13280-017-0958-y.

[35] D. Isleifson, R. J. Galley, D. G. Barber, J. C. Landy, A. S. Komarov, and L. Shafai, "A study on the C-band polarimetric scattering and physical characteristics of frost flowers on experimental sea ice," *IEEE Trans. Geosci. Remote Sens.*, vol. 52, no. 3, pp. 1787–1798, Mar. 2014, doi: 10.1109/TGRS.2013.2255060.

[36] R. J. Galley et al., "Micrometeorological and thermal control of frost flower growth and decay on young sea ice," *Arctic*, vol. 68, no. 1, pp. 79–92, 2015, doi: 10.14430/arctic4457.

[37] F. Ulaby and D. Long, *Microwave Radar and Radiometric Remote Sensing*. Ann Arbor, MI, USA: Univ. of Michigan Press, 2014.

[38] J. B. Mead, "C-band and Ku-band polarimetric scatterometer: Operations manual," ProSensing Inc., Amherst, MA, USA, Revision A, Tech. Rep., Nov. 2019, pp. 1–61.

[39] T. Geldsetzer, J. B. Mead, J. J. Yackel, R. K. Scharien, and S. E. L. Howell, "Surface-based polarimetric C-band scatterometer for field measurements of sea ice," *IEEE Trans. Geosci. Remote Sens.*, vol. 45, no. 11, pp. 3405–3416, Nov. 2007, doi: 10.1109/TGRS.2007.907043.

[40] S. R. Cloude and E. Pottier, "A review of target decomposition theorems in radar polarimetry," *IEEE Trans. Geosci. Remote Sens.*, vol. 34, no. 2, pp. 498–518, Mar. 1996, doi: 10.1109/36.485127.

[41] M. E. Shokr, L. J. Wilson, and D. L. Surdu-Miller, "Effect of radar parameters on sea ice tonal and textural signatures using multi-frequency polarimetric SAR data," *Photogramm. Eng. Remote Sens.*, vol. 61, no. 12, pp. 1463–1473, 1995.

[42] B. Scheuchl, I. Hajnsek, and I. G. Cumming, "Model-based classification of polarimetric SAR sea ice data," in *Proc. IEEE Int. Geosci. Remote Sens. Symp. (IGARSS)*, vol. 3, Jun. 2002, pp. 1521–1523, doi: 10.1109/IGARSS.2002.1026168.

[43] H. Israelsson and J. Askne, "Analysis of polarimetric SAR observations of sea ice," in *Proc. Remote Sens., Global Monit. Earth Manage. (IGARSS)*, vol. 1, Jun. 1991, pp. 89–92, doi: 10.1109/IGARSS.1991.577674.

[44] T. Geldsetzer and J. J. Yackel, "Sea ice type and open water discrimination using dual co-polarized C-band SAR," *Can. J. Remote Sens.*, vol. 35, no. 1, pp. 73–84, Jan. 2009, doi: 10.5589/m08-075.

[45] M. Shokr and N. Sinha, *Sea Ice: Physics and Remote Sensing*. Hoboken, NJ, USA: Wiley, 2015.

[46] S. Skrunes, C. Brekke, and T. Eltoft, "Characterization of marine surface slicks by Radarsat-2 multipolarization features," *IEEE Trans. Geosci. Remote Sens.*, vol. 52, no. 9, pp. 5302–5319, Sep. 2014, doi: 10.1109/TGRS.2013.2287916.

[47] M. Migliaccio, F. Nunziata, and A. Buono, "SAR polarimetry for sea oil slick observation," *Int. J. Remote Sens.*, vol. 36, no. 12, pp. 3243–3273, Jun. 2015, doi: 10.1080/01431161.2015.1057301.

[48] W. Dierking and C. Wesche, "C-band radar polarimetry—Useful for detection of icebergs in sea ice?" *IEEE Trans. Geosci. Remote Sens.*, vol. 52, no. 1, pp. 25–37, Jan. 2014, doi: 10.1109/TGRS.2012.2234756.

[49] B. Scheuchl, I. Hajnsek, and I. Cumming, "Sea ice classification using multi-frequency polarimetric SAR data," in *Proc. IEEE Int. Geosci. Remote Sens. Symp. (IGARSS)*, vol. 3, Jun. 2002, pp. 1914–1916, doi: 10.1109/IGARSS.2002.1026298.

[50] J.-S. Lee, M. R. Grunes, T. L. Ainsworth, L.-J. Du, D. L. Schuler, and S. R. Cloude, "Unsupervised classification using polarimetric decomposition and the complex Wishart classifier," *IEEE Trans. Geosci. Remote Sens.*, vol. 37, no. 5, pp. 2249–2258, Sep. 1999, doi: 10.1109/36.789621.

[51] E. Pottier and J. S. Lee, "Unsupervised classification scheme of PolSAR images based on the complex Wishart distribution and the H/A/α polarimetric decomposition theorem," in *Proc. EUSAR*, 2000, pp. 265–268.

[52] S.-E. Park and W. M. Moon, "Unsupervised classification of scattering mechanisms in polarimetric SAR data using fuzzy logic in entropy and alpha plane," *IEEE Trans. Geosci. Remote Sens.*, vol. 45, no. 8, pp. 2652–2664, Aug. 2007, doi: 10.1109/TGRS.2007.897691.

[53] W. Dierking, H. Skriver, and P. Gudmandsen, "SAR polarimetry for sea ice classification," Eur. Space Agency, Paris, France, ESA SP 529, 2003, pp. 109–118.

[54] Meteorological Service of Canada, *MANICE: Manual of Standard Procedures for Observing and Reporting Ice Conditions*, 9th ed. Ottawa, ON, Canada: Environment Canada, 2005.

[55] D. G. Barber, "Microwave remote sensing, sea ice and Arctic climate," *Phys. Canada*, pp. 105–111, Oct. 2005.

[56] B. Scheuchl, I. Hajnsek, and I. Cumming, "Classification strategies for polarimetric SAR sea ice data," Eur. Space Agency, Paris, France, Tech. Rep. ESA SP 529, 2003.

[57] M. M. Espeseth, C. Brekke, C. E. Jones, B. Holt, and A. Freeman, "The impact of system noise in polarimetric SAR imagery on oil spill observations," *IEEE Trans. Geosci. Remote Sens.*, vol. 58, no. 6, pp. 4194–4214, Jun. 2020, doi: 10.1109/TGRS.2019.2961684.

[58] D. Barber. (2014). The Churchill marine observatory. Centre of Earth Observation Science. Accessed: Mar. 10, 2020. [Online]. Available: https://umanitoba.ca/faculties/environment/departments/ceos/media/CMO_full_proposal_F.pdf
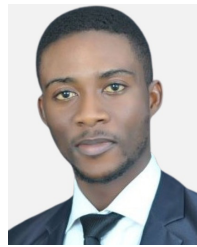
Elvis Asihene (Graduate Student Member, IEEE) received the B.Sc. degree in geological engineering from the Ghana's University of Mines and Technology, Tarkwa, Ghana, in 2011, and the M.Sc. degree in applied geophysics from the University of Ghana, Accra, Ghana, in 2017. He is currently pursuing the Ph.D. degree in geography with the University of Manitoba, Winnipeg, MB, Canada.

His main areas of research are in arctic science, remote sensing, and GIS. He is particularly interested in using microwave remote sensing to detect oil spills in Arctic ice-covered waters. His other research interests include electromagnetic modeling and inversion of sea ice-related parameters, and the application of polarimetry and interferometry radar for target characterization and surface subsidence, respectively.

Gary Stern received the Ph.D. degree in chemistry on mass spectrometry from the University of Manitoba, Winnipeg, MB, Canada, in 1991.

He is currently a Professor with the Centre for Earth Observations Sciences, University of Manitoba. He is currently the Co-Lead of the GENICE II Project that involves genomics research in oil spill preparedness and emergency response in an Arctic marine environment. He was involved in the study of environmental pathways of contaminants in Arctic marine and freshwater ecosystems. He is involved in the development of oil detection and remediation technologies, impacts, and fate of oil spills in Arctic marine environments.
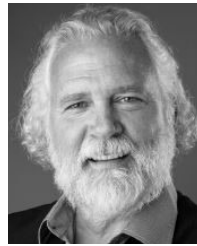
David G. Barber received the Ph.D. degree from the University of Waterloo, Waterloo, ON, Canada, in 1992.

Since 1993, he has been a Professor with the University of Manitoba, Winnipeg, MB, Canada, and became the Canada Research Chair in Arctic System Science in 2002. He has authored or coauthored over 240 articles and has been a scientific leader in large network programs (NOW, CASES, ArcticNet, CFL, BaySys, and CMO).

Dr. Barber is an Invited Member of several national (NSERC GSC 09, NSERC IPY, and NSERC Northern Supplements) and international (GEWEX, IAPP, CNC-SCOR, and IARC) committees. He is a fellow of the Royal Society of Canada (Science Academy), an Officer of the Order of Canada, and a UM Distinguished Professor.
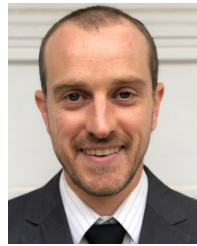
Colin Gilmore (Senior Member, IEEE) is the Tier 2 Canada Research Chair in Applied electromagnetic inversion and an Assistant Professor of electrical and computer engineering with the University of Manitoba, Winnipeg, MB, Canada. His research interests include the systems and algorithms of sensing objects with electromagnetic waves and biomedical imaging for cancer detection, geophysical images, to imaging the contents of grain storage bins.

Dustin Isleifson (Senior Member, IEEE) received the Ph.D. degree in electrical and computer engineering from the University of Manitoba, Winnipeg, MB, Canada, in 2011.

From 2013 to 2016, he was an Electrical Engineer with Magellan Aerospace, Winnipeg, where he worked on the Radarsat Constellation Mission (RCM). He has been with the Department of Electrical and Computer Engineering and the Centre for Earth Observation Science (CEOS), University of Manitoba, as an Assistant Professor in 2016, and as an Associate Professor in 2022. His research interests include remote sensing, Arctic science, antenna design, and satellite technologies.

Dr. Isleifson is the Chapter Chair of the Winnipeg Section of the IEEE TRANSACTIONS ON GEOSCIENCE AND REMOTE SENSING (GRS) and IEEE TRANSACTIONS ON AEROSPACE AND ELECTRONIC SYSTEMS (AES).